Springer

KSME

Journal of Mechanical Science and Technology 29 (4) (2015) 1513~1526
www.springerlink.com/content/1738-494x
DOI 10.1007/s12206-015-0324-6

Characteristics analysis of blade-casing rubbing based on casing vibration acceleration †

G. Chen*

College of Civil Aviation, Nanjing University of Aeronautics and Astronautics, Nanjing, 210016, China

(Manuscript Received August 11, 2014; Revised October 27, 2014; Accepted December 22, 2014)

Abstract

Blade-casing rubbing experiments, which include single-point rubbing and partial rubbing, are carried out on an aero engine rotor experimental rig with casings. Casing vibration acceleration signals are analyzed for extracting the rubbing faults' characteristics. The results show that under rubbing, casing signals have obvious impact characteristics: impact frequency is the frequency of blades passing the casing, and it equals the product of rotating frequency and the number of blades; the frequency spectrum shows the blade-passage frequency and its multiple-frequencies; impact strength is modulated by the rotating frequency so that there are families of side bands on both sides of the blade-passage frequency and its multiple frequencies, and the side bands' interval equals the rotating frequency. There are obvious quefrency components of the rotating frequency and its multiple frequencies in the cepstrum, and there is also a distinct rotating frequency and its multiple frequencies in the wavelet envelope spectrum. Finally, the rubbing characteristics determined in this study are verified by using test data from an actual aero engine.

Keywords: Aero engine; Blade-casing rubbing; Casing acceleration; Characteristics analysis; Cepstrum; Wavelet envelope spectrum

1. Introduction

For improving the thrust–weight ratio and structural efficiency of an aero engine, the clearance between its rotor and stator needs to be narrowed. However, by doing so, the possibility of rotor–stator rubbing, especially blade–casing rubbing, will increase greatly. Rotor–stator rubbing can have dire consequences, such as rotor–stator clearance enlargement, bearing wear, blade breakage, and even overall mechanical failure [1, 2].

Many studies have been conducted on the rubbing dynamics mechanism and rubbing experiments; a few characteristics and phenomena ascribed to rubbing, such as waveform cutting, frequency doubling, frequency division, and chaos, have been determined. In many such studies, theoretically deduced results were verified experimentally [3-9]. Recent studies on rubbing faults have considered the structural features of actual blades. Liu et al. [10] conducted a numerical simulation of the aero engine blade–casing rubbing process using LS-DYNA, a general-purpose finite element software program, and analyzed the dynamic response on the top of a blade under the combined effect of instant crash and friction load (Rubbing load), while considering the structural features of actual blades. Williams [11] proposed a new modeling method for blade–casing rubbing. This model incorporates a refined model of inner wear in casing, and the applicability of this method is verified by an experiment. By analyzing the blade-casing local contact rubbing force data obtained from experiments and contact dynamics simulation, it can be found that the contact force of single-point rubbing or local rubbing is similar to a periodic pulse force. Considering this rubbing condition, a few have proposed simulation methods for rubbing faults based on the pulse force model [12-14].

However, for aero engines, the main distinctions of rubbing faults are as follows: 1) casings are typical thin-walled structures; 2) rubbing faults mainly appear between the blade and the casing; 3) generally, only vibration acceleration of the casing can be measured, and it is very difficult to obtain vibration displacement of rotors; therefore, it is impossible to recognize the rubbing faults through the rotors' vibration signal characteristics.

The existing theoretical and experimental studies do not consider all of the above-mentioned characteristics. Consequently, they cannot be applied directly to aero engine rubbing fault diagnosis. It is necessary to study the characteristics and laws of casing vibration acceleration signals for effectively identifying the rubbing faults of an aero engine. In addition, some experimental work is carried out for analyzing and verifying the characteristics of blade–casing rubbing faults.

*Corresponding author. Tel.: +86 25 84891850, Fax.: +86 25 84891850
E-mail address: cgzyx@263.net
† Recommended by Associate Editor Cheolung Cheong

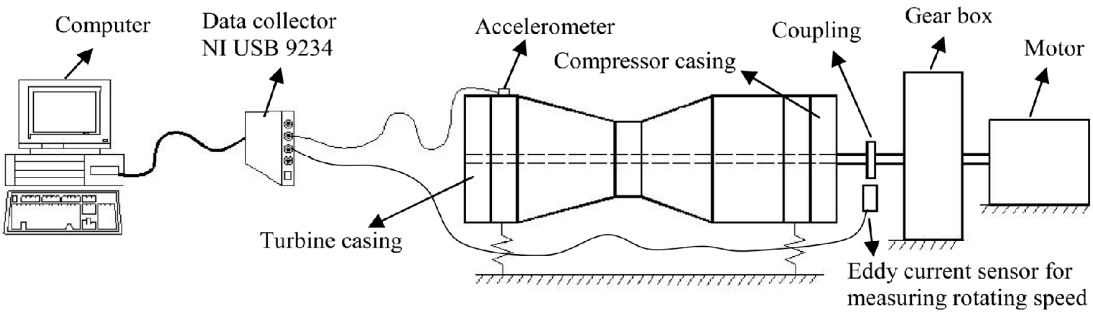

Fig. 1. The rubbing experiment diagram.

In this study, an aero engine rotor experimental rig is used for single-point and local partial rubbing experiments. The casing vibration acceleration signals are measured and analyzed, and the characteristics and laws of blade–casing rubbing faults are found. Finally, the characteristics are verified with real aero engine test data.

2. Analysis of rubbing fault characteristics based on rubbing experiments

2.1 Introduction to aero engine rotor experiment rig

We used an aero engine rotor experiment rig with shaft, ball bearings, discs, blades and thin-walled casings, designed by the Shenyang Aero-engine Design Institute, China, for the rubbing experiments. The structural design of this experimental rig has these features as follows: First, its shape is consistent with that of core-engine casings, and its size is treble reduced. Second, the internal structure of the rig is simplified. The core-engine is simplified to a 0-2-0 support structure form, and an adjustable stiffness support structure is designed for adjusting the system's dynamic characteristics. Third, the multistage compressor is simplified to a single-stage disk structure. Finally, the aero engine experimental rig forms the rotor-support-blade disk-casing system.

The experiment diagram is shown in Fig. 1, the aero engine rotor experiment rig is driven by the motor, and the rotating speed is increased by the gear box. The rubbing experiments are made on the turbine casing. In the experiments, rubbing bolts are screwed using a spanner for deforming the rubbing loop so that single-point rubbing appears between the rubbing loop and the rotating turbine blades. The bearing housing position can be adjusted using a turbine screw mechanism so that the entire rotor moves to the casing and partial blade–casing rubbing takes place. Rubbing sparks occur under intense rubbing. The vibration signals on the turbine casing are collected by means of the USB9234 data acquisition card of the NI Company; the 4805 type ICP acceleration sensors of B&K Company are used to pick up the acceleration signals, and the eddy current sensor is used to measure the rotating speed. The sampling frequency is 10.24 kHz.

The average wall thickness is 7 mm, whereas that of typical thin-walled casings is 4 mm. The thick-walled turbine casing

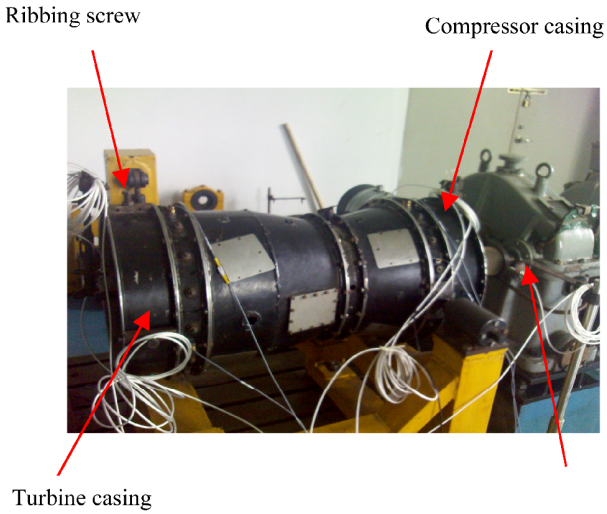

Fig. 2. Aero engine rotor experimental rig.

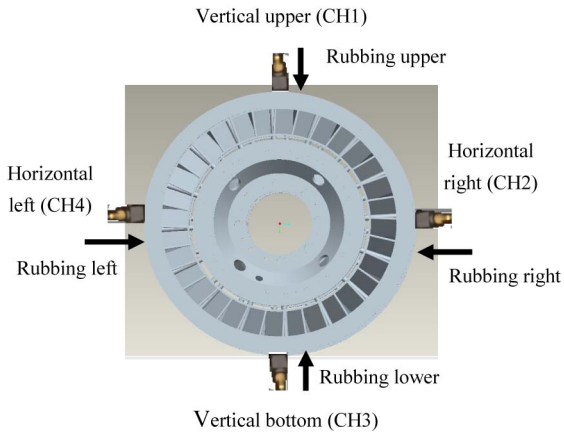

Fig. 3. Radial measurement points and rubbing points on turbine casing.

photograph before installation is shown in Fig. 6, and its physical map after installation is shown in Fig. 7. The single-point rubbing experiment conducted on the thick-walled casing is shown in Fig. 8. A schematic diagram of the rubbing measurement points on the thick-walled turbine casing is shown in Fig. 8. A comparison of Figs. 3 and 9 shows that unlike the thin-walled casing, on the thick-walled casing, the

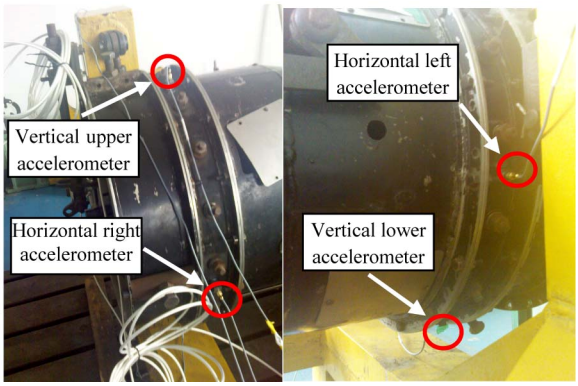

Fig. 4. Accelerometers on turbine casing.

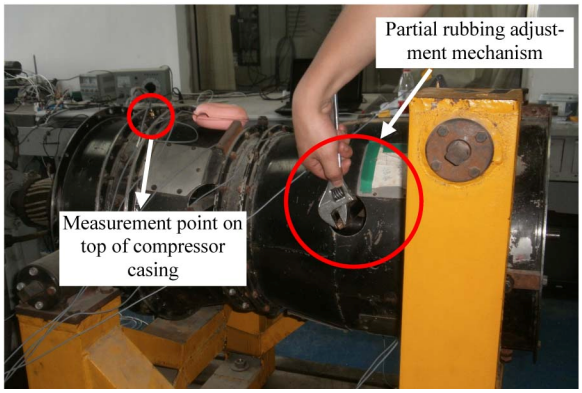

Fig. 5. Partial rubbing adjustment mechanism.

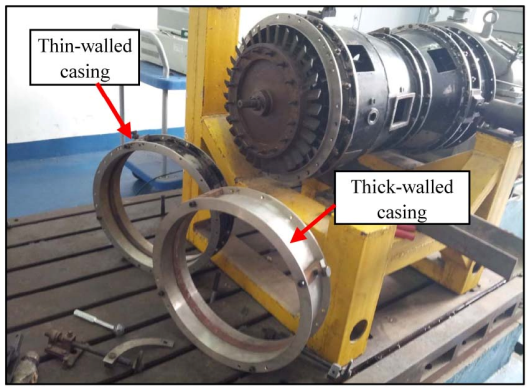

Fig. 6. Thick-walled casing before installation.

Fig. 7. Thick-walled casing after installation.

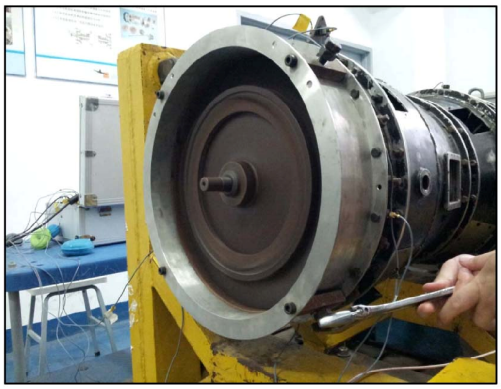

Fig. 8. Single-point rubbing of thick-walled casing.

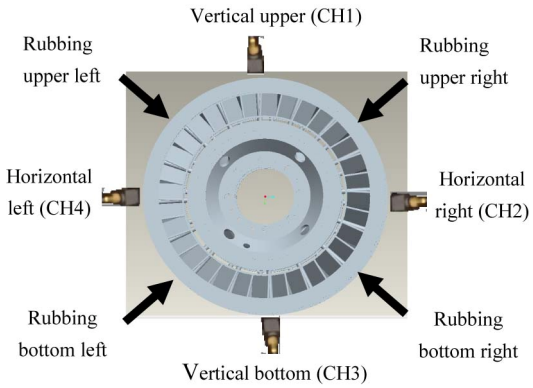

Fig. 9. Radial measurement points and rubbing points on thick-walled turbine casing.

single-point rubbing positions are at the upper right, bottom right, bottom left, and upper left. However, the positions of partial rubbing are the same as those on the thin-walled casing.

As can be seen in Fig. 5, partial blade-casing rubbing is achieved by moving the shaft-disc-blades in the left or the right direction after screwing the partial rubbing adjustment mechanism.

For comparing the effect of casing thickness on rubbing fault characteristics, a thick-walled turbine casing is designed. The average wall thickness is 7 mm, whereas that of typical thin-walled casings is 4 mm. The thick-walled turbine casing photograph before installation is shown in Fig. 6, and its physical map after installation is shown in Fig. 7. The single-point rubbing experiment conducted on the thick-walled casing is shown in Fig. 8. A schematic diagram of the rubbing measurement points on the thick-walled turbine casing is shown in Fig. 8. A comparison of Figs. 3 and 9 shows that unlike the thin-walled casing, on the thick-walled casing, the single-point rubbing positions are at the upper right, bottom right, bottom left, and upper left. However, the positions of partial rubbing are the same as those on the thin-walled casing.

Table 1. Rubbing experiment data.

Experiment date	Rubbing type	Rubbing intensity	Turbine casing	Measurement points	Rotational speed
2011-07-27	Single point	Light; intense	Thin-walled (4 mm)	Turbine casing: top, right, bottom, and left	1000 rpm 1700 rpm
2012-05-12	Single point	Moderate	Thin-walled (4 mm)	Turbine casing: top, right, bottom, and left	1500 rpm
2013-04-29	Single point, partial	Moderate	Thin-walled (4 mm)	Turbine casing: top, right, bottom, and left; compressor casing: top	1200 rpm
2013-06-26	Single point, partial	Moderate	Thick-walled (7 mm)	Turbine casing: top, right, bottom, and left; compressor casing: top	1200 rpm

The data of four experiments conducted on July 27, 2011, May 12, 2012, April 29, 2013, and June 26, 2013 were selected for analysis and summarized in Table 1. The experiments conducted on July 27, 2011 were single-point rubbing on a thin-walled turbine casing. The measurement points on the turbine casing were the top, right, bottom, and left; the rubbing intensities were light and intense at rotational speeds of 1000 rpm and 1700 rpm, respectively. The experiments conducted on May 12, 2012 were single-point rubbing on the thin-walled turbine casing. The measurement points on the turbine casing were the top, right, bottom, and left, and the rubbing intensity was moderate at the rotational speed of 1500 rpm. The experiments conducted on April 29, 2013 were single-point and partial rubbing on the thin-walled turbine casing. The measurement points on the turbine casing were the top, right, bottom, and left, and top on the compressor casing. The rubbing intensity was moderate at the rotational speed of 1200 rpm. The experiments conducted on June 26, 2013 were single-point and partial rubbing on the thick-walled turbine casing. The measurement points on the turbine casing were the top, right, bottom, and left, and top on the compressor casing. The rubbing intensity was moderate at the rotational speed of 1200 rpm.

2.2 Characteristics analysis of casing acceleration signals under single-point rubbing

Channel 1 (CH1) testing data obtained from the experiments conducted on May 12, 2012, is selected; the corresponding rubbing position is the vertical top, and the experimental rotational speed is 1489 rpm (= 24.8 Hz). Figs. 10(a) and (b) show the time-domain waveforms; Fig. 10(b) is an enlarged version of Fig. 10(a). The frequency spectrum plots are shown in Figs. 10(c)-(e); Fig. 10(e) is enlargement 1 of Figs. 10(c) and (d) is enlargement 2 of Fig. 10(c). Fig. 10(f) shows the signal cepstrum. Figs. 10(g) and (h) shows the wavelet envelope spectrums.

The cepstrum, which is a very useful diagnosis method in engineering practice, is defined as the inverse Fourier transform after taking the logarithm of the power spectral density function, as shown in Eq. (1), in which IDFT[.] denotes the inverse discrete Fourier transform; the total number of the discrete frequency point is N, and $k = 1,2,\ldots N$; $S_{xx}(k)$ is the power spectral density function; therefore, the cepstrum is:

$$C_x(k) = IDFT[\lg(S_{xx}(k))] . \quad (1)$$

An important role of the cepstrum is to analyze the amplitude modulation signal such as faulty gear vibration signal; its effectiveness has already been verified by many engineering cases. The cepstrum can simplify a group of sideband frequency bands in original power spectrum into some single spectral lines, and the quefrency of the first single spectral line is the reciprocal of the frequency interval of the sidebands.

In this study, a new method to analyze the amplitude modulation signal is carried out by means of a wavelet envelope spectrum analysis. Qiu [15] provides a reference for the detailed process of this algorithm. The essence of wavelet envelope spectrum analysis is to take advantage of the bandpass filter characteristics of wavelet analysis, and to decompose the signals using appropriate wavelet functions so as to obtain an appropriate frequency band. Then, by means of envelope demodulation, low frequency envelop signals that only contain the modulation information are obtained. Its spectrum is the wavelet envelope spectrum, in which the modulation frequencies of the signals can be found. In this paper, the multi resolution wavelet analysis method and the Db4 wavelet function are selected; the number of the decomposition levels is 3, and those decomposition signals can be obtained, which include the first layer detail signal d1, the second layer detail signal d2, the third layer detail signal d3, and the third layer approximation signal a3. Figs. 10(g) and (h) are wavelet envelope spectrums of the first layer detail signal d1 and the second layer detail signal d2.

Because the rotor experiment rig is a shaft-disk-blade structure, when rubbing occurs, every blade hits the rubbing point in turn. This impact action circulates once for each complete rotor rotation. Therefore, the impact frequency due to rubbing is the frequency at which the blades pass the rubbing point on the casing, and it is blade-passage frequency, and equals the

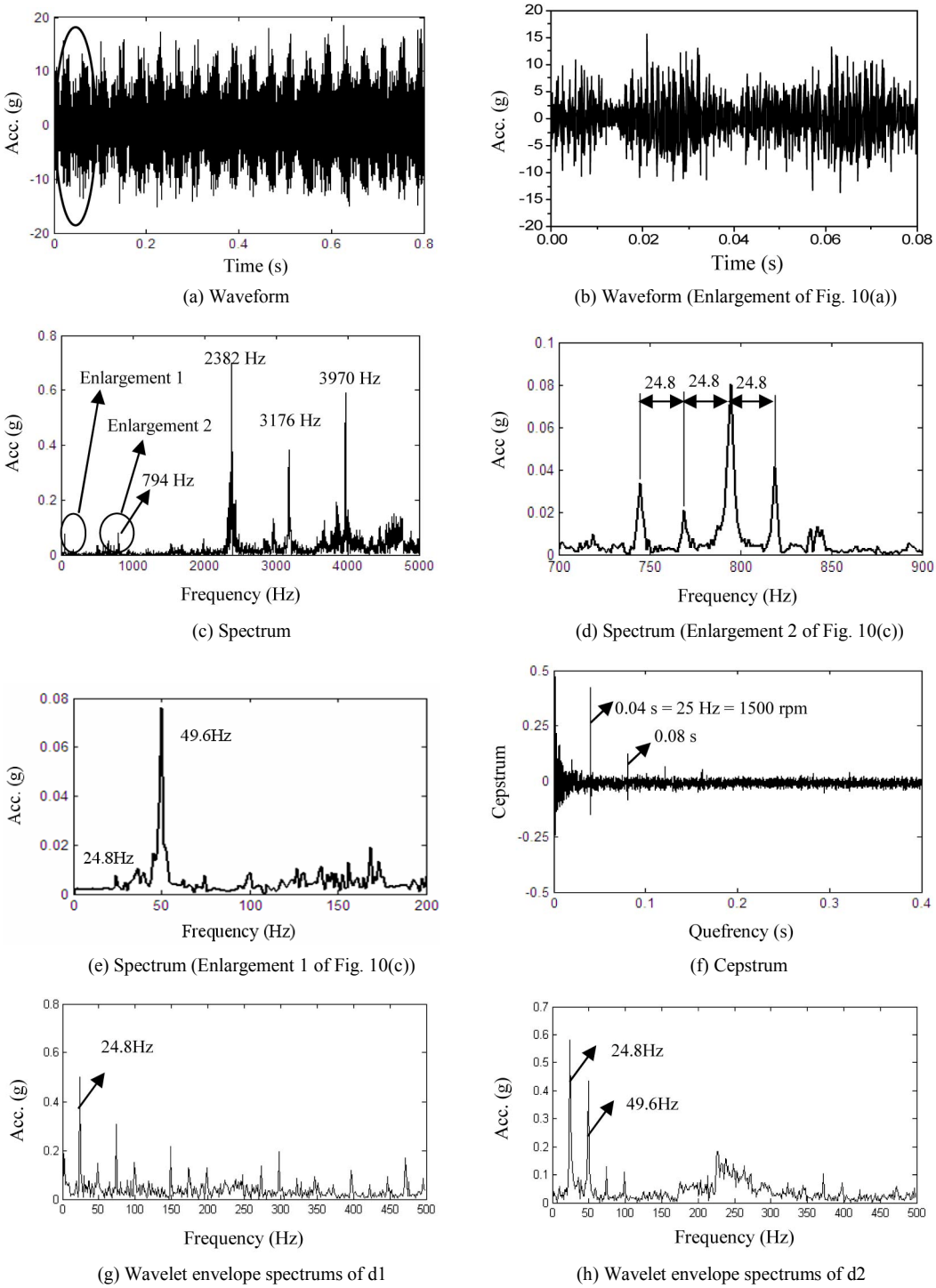

(a) Waveform

(b) Waveform (Enlargement of Fig. 10(a))

(c) Spectrum

(d) Spectrum (Enlargement 2 of Fig. 10(c))

(e) Spectrum (Enlargement 1 of Fig. 10(c))

(f) Cepstrum

(g) Wavelet envelope spectrums of d1

(h) Wavelet envelope spectrums of d2

Fig. 10. Characteristics analysis under single-point rubbing.

product of rotating frequency and the number of blades. Therefore, the frequency spectrum shows the impact frequency and its multiple frequencies. In addition, under excitation from an unbalanced force, the rotor produces a whirling motion with a frequency equal to the rotating frequency; consequently, the strength of the impact action of rubbing is modulated by the rotational frequency. Therefore, there are the obvious amplitude modulation characteristics in the frequency spectrum, i.e., there are many side bands on both sides of the blade-passage frequency and its multiple frequencies. In the experimental data, the rotational speed is 1489 rpm, rotational frequency is 24.8 Hz, and the number of blades is 32; therefore, the rubbing frequency is 794 Hz, which is the product of the rotational frequency and the number of blades. The rub-

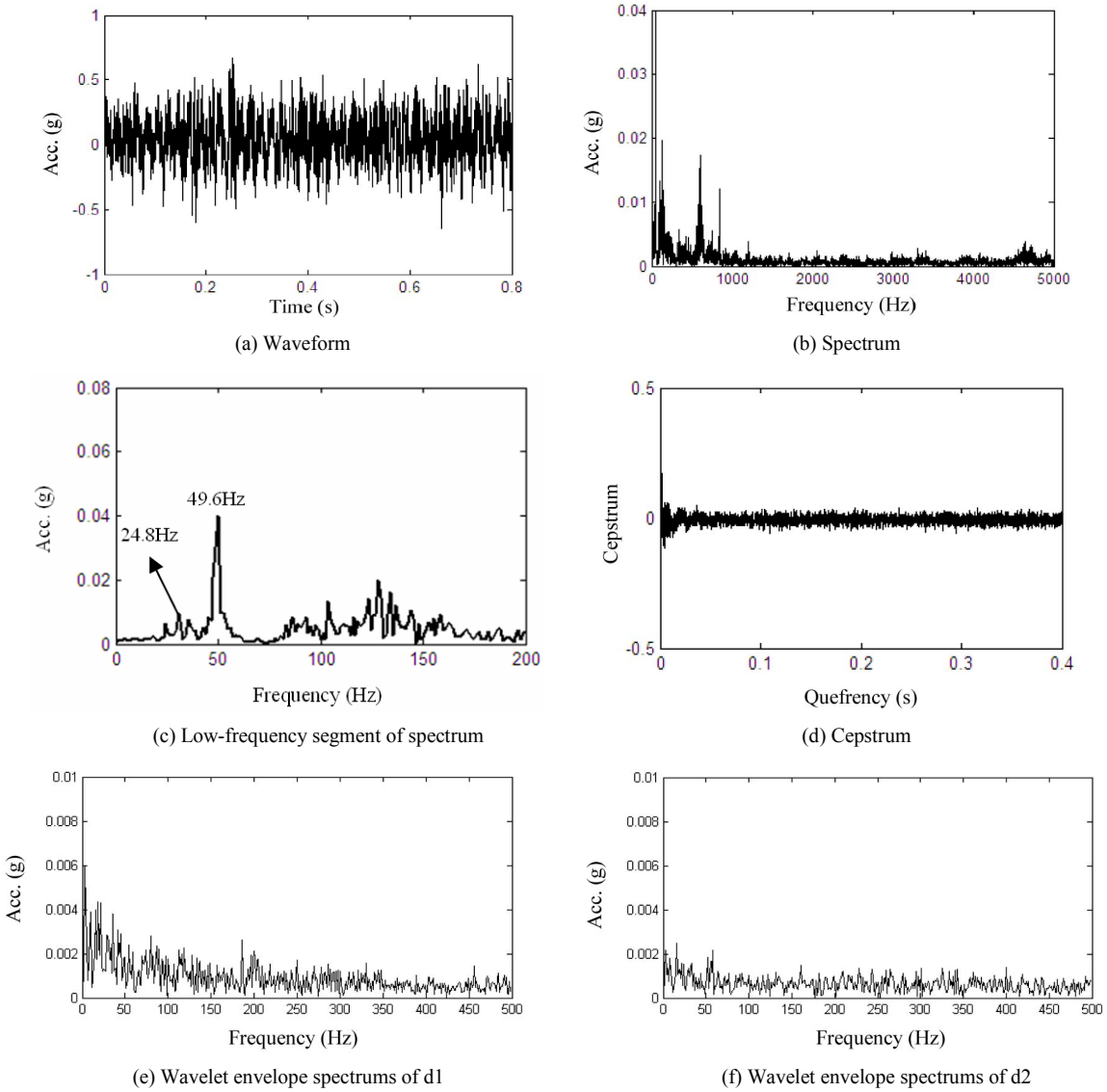

(a) Waveform

(b) Spectrum

(c) Low-frequency segment of spectrum

(d) Cepstrum

(e) Wavelet envelope spectrums of d1

(f) Wavelet envelope spectrums of d2

Fig. 11. Characteristics analysis under no rubbing.

bing frequency and its multiple frequencies (794 Hz, 1588 Hz, 2382 Hz, 3176 Hz, and 3970 Hz), are shown in Fig. 10(c). There are side bands on both sides of blade-passage frequency and its multiple frequencies, and the side bands' interval is equal to the rotational frequency, which is 24.8 Hz in this case. Fig. 10(d) zooms in on the spectrum near 749 Hz. From this figure, the side bands near 749 Hz can be observed, and the side bands' interval equals the rotational frequency. Furthermore, there are obvious quefrency components of the rotational frequency and its multiple frequencies, as shown in Fig. 10(f). Fig. 10(e) shows the low-frequency segment of the spectrum, the rotational frequency, and its multiple frequency components. In addition, in the wavelet envelope spectrums as shown in Figs. 10(g) and (h), there is a very obvious rotational frequency and its multiple frequencies components, and it also shows that the casing acceleration signal is modulated by the rotational frequency.

For the sake of comparison, under no rubbing, the testing data of CH1 obtained from the experiments conducted on May 12, 2012, is selected. Fig. 11(a) shows the time-domain waveforms, Fig. 11(b) shows the frequency spectrum, Fig. 11(c) shows the low-frequency segment of spectrum, Fig. 11(d) shows the cepstrum, Figs. 11(e) and (f) are the wavelet envelope spectrums of d1 and d2. Compared with the acceleration signals of the casing under rubbing, it can be seen that under no rubbing, the blade-passage frequency and its multiple frequencies do not appear, and there are no amplitude modulation characteristics in the signals, as well as no quefrency components of the rotational frequency and its multiple frequencies in the cepstrum, and there is no rotational frequency and its multiple frequencies in the wavelet envelope spectrum. Additionally, in the low-frequency segment, the multiple frequency components of the rotational frequency are more obvious under rubbing than under no rubbing.

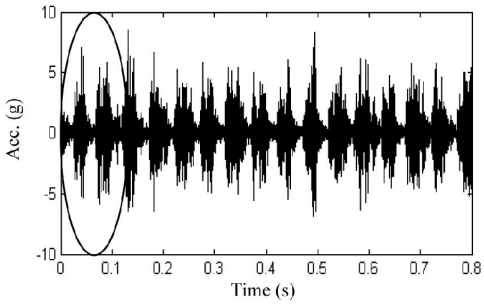

(a) Time-domain waveform

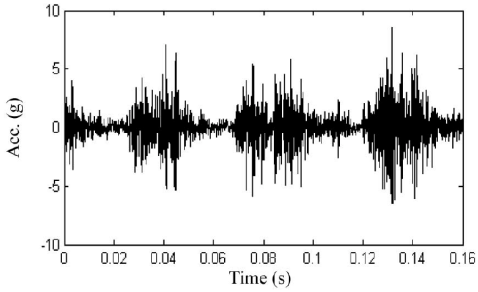

(b) Time-domain waveform (Enlargement of Fig. 12(a))

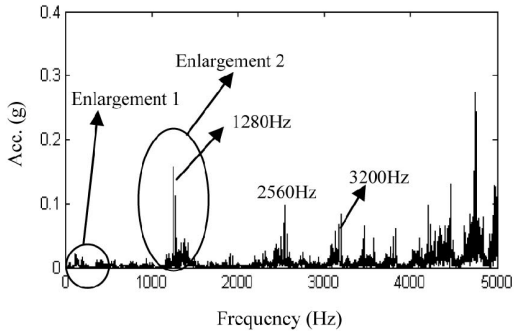

(c) Spectrum

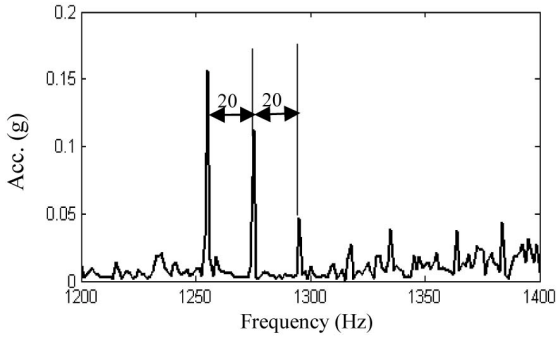

(d) Spectrum (Enlargement 2 of Fig. 12(c))

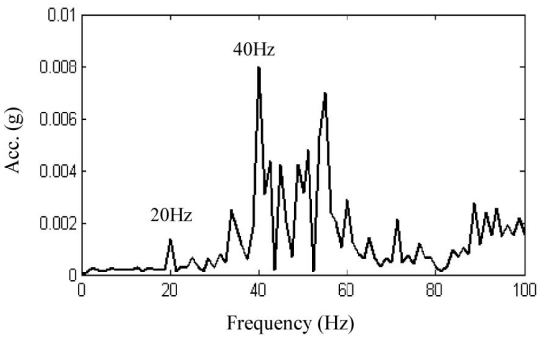

(e) Spectrum (Enlargement 1 of Fig. 12(c))

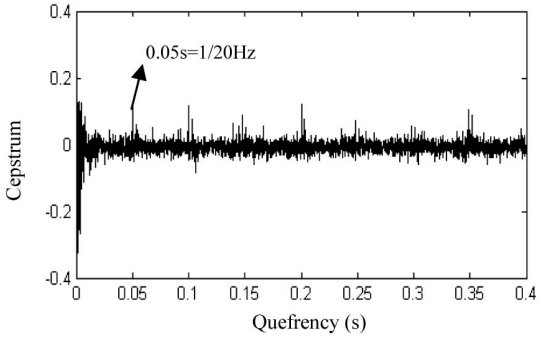

(f) Cepstrum

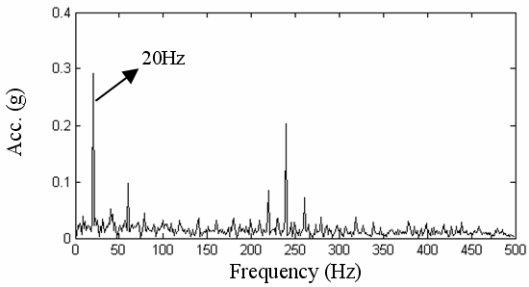

(g) Wavelet envelope spectrums of d1

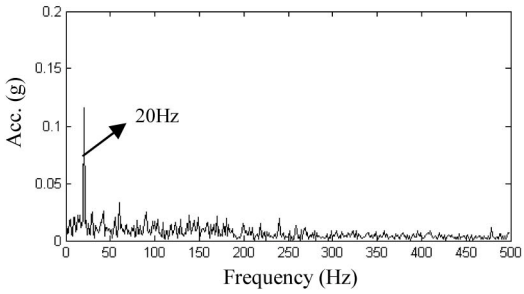

(h) Wavelet envelope spectrums of d2

Fig. 12. Characteristics analysis under partial rubbing.

2.3 Analysis of casing acceleration signals under partial rubbing

The testing data of CH1 obtained from the experiments conducted on April 29, 2013 is selected. The rotor–stator rubbing position was at the horizontal right. The experimental rotational speed was 1199 rpm = 20 Hz. Figs. 12(a) and (b) show the time-domain waveforms, and Fig. 12(b) shows an enlarged version of Fig. 12(a). Figs. 12(c)-(e) show the frequency spectrum plots. Fig. 12(e) is enlargement 2 of Fig. 12(c), while Fig. 12(d) is an enlargement 1 of Fig. 12(c). Fig. 12(f) shows the signal cepstrum. Figs. 12(e) and (f) are the wavelet envelope spectrums of d1 and d2.

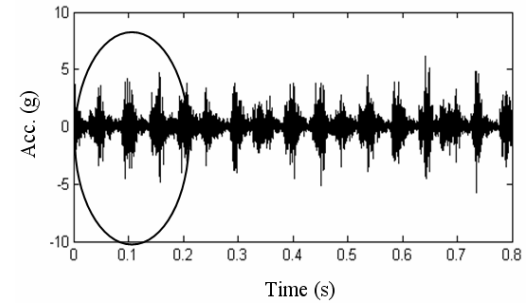

(a) Time-domain waveform

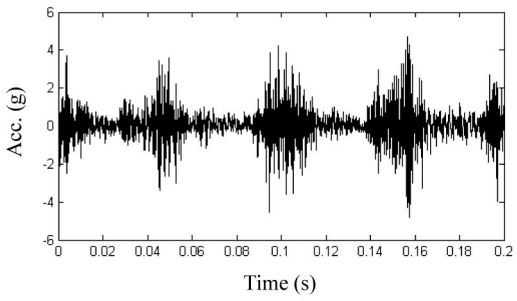

(b) Time-domain waveform (Enlarged Fig. 13(a))

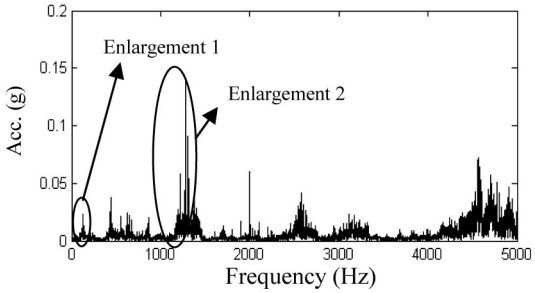

(c) Spectrum

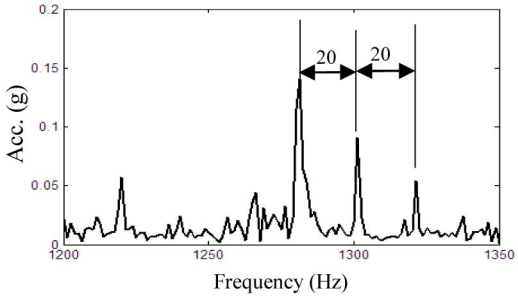

(d) Spectrum (Enlarged 2 of Fig. 13(c))

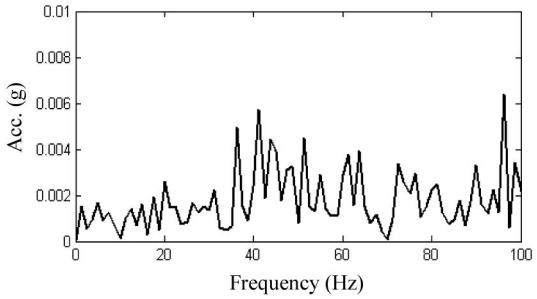

(e) Spectrum (Enlarged 1 of Fig. 13(c))

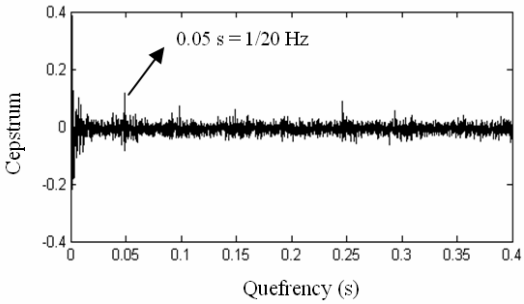

(f) Cepstrum

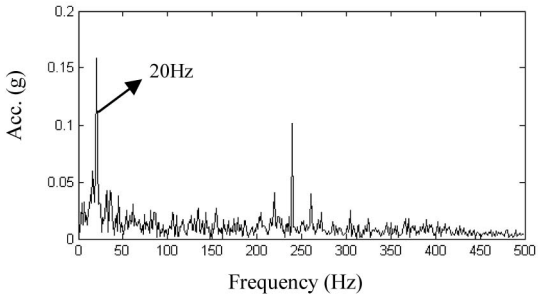

(g) Wavelet envelope spectrums of d1

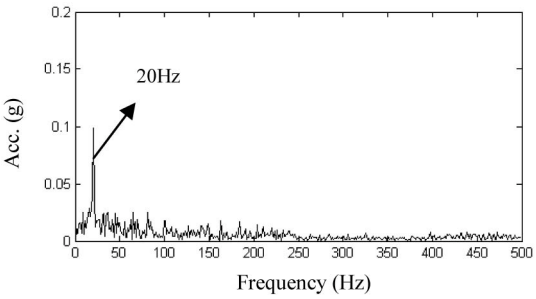

(h) Wavelet envelope spectrums of d2

Fig. 13. Characteristics analysis under thick casing.

From these figures, it can be seen that the characteristics of the casing vibration acceleration signals under partial rubbing are the same as those under single-point rubbing. The casing signals under partial rubbing have obvious impact characteristics, which can be ascribed to the blade-passage frequency and its multiple frequencies. Impact strength is modulated by the rotational frequency, and there are obvious quefrency components of the rotational frequency and its multiple frequencies in the cepstrum, and there also are obvious rotational frequency component in the wavelet envelope spectrums.

2.4 Effect of casing thickness on rubbing characteristics

For comparing the effect of casing thickness on rubbing fault characteristics, the testing data of CH1 obtained from the experiments conducted on June 26, 2013 was selected,

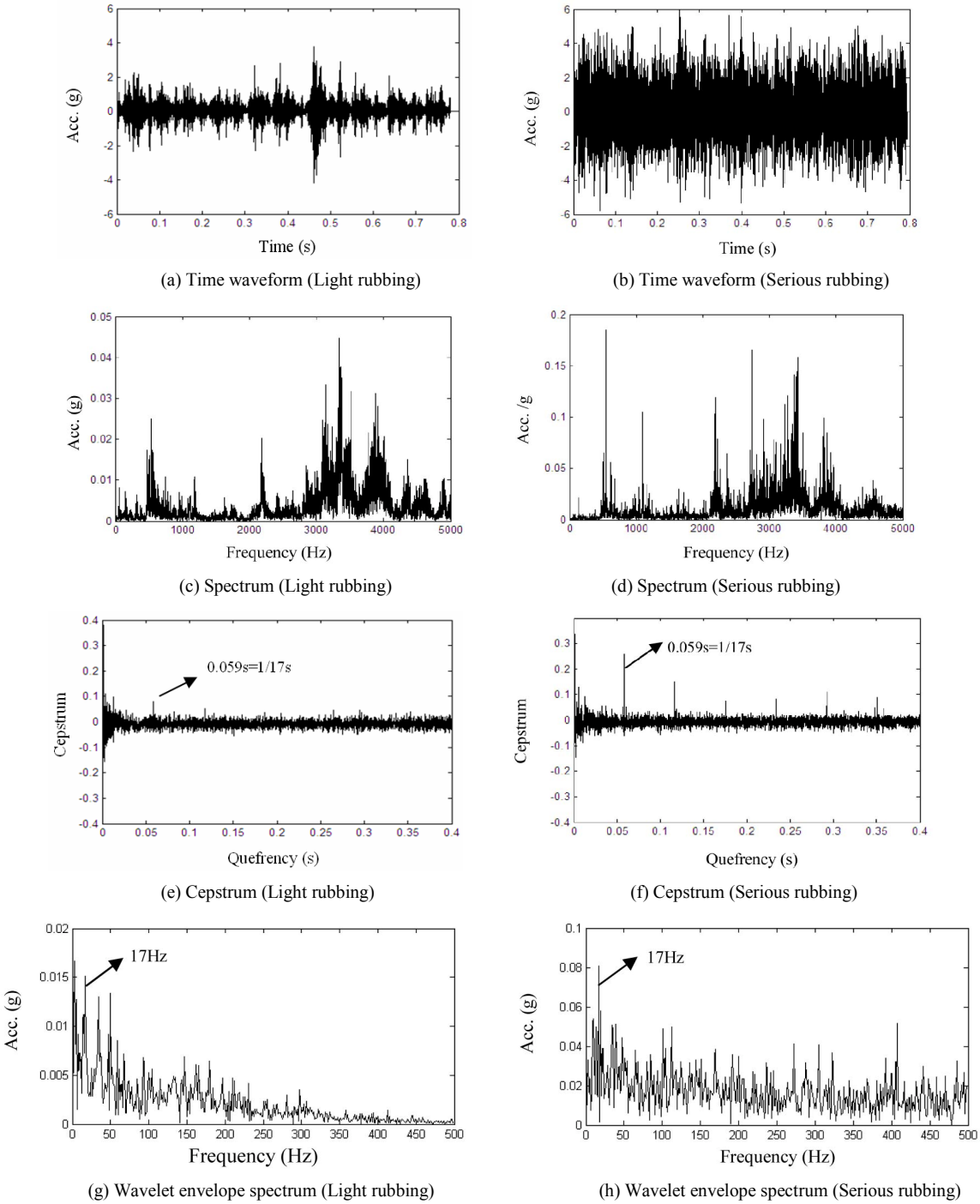

(a) Time waveform (Light rubbing)

(b) Time waveform (Serious rubbing)

(c) Spectrum (Light rubbing)

(d) Spectrum (Serious rubbing)

(e) Cepstrum (Light rubbing)

(f) Cepstrum (Serious rubbing)

(g) Wavelet envelope spectrum (Light rubbing)

(h) Wavelet envelope spectrum (Serious rubbing)

Fig. 14. Characteristics analysis under different rubbing intensity.

and the rotor–stator rubbing position was the top right of the thick-walled turbine casing. The experimental rotational speed was 1220 rpm = 20 Hz. Figs. 13(a) and (b) show the time-domain waveforms, and Fig. 13(b) shows an enlarged version of Fig. 13(a). Figs. 13(c)-(e) show the frequency spectrum plots; Figs. 13(d) and (e) are enlargements 2 and 1, respectively, of Fig. 13(c). Fig. 13(f) shows the signal cepstrum. Figs. 13(g) and 12(h) are the wavelet envelope spectrums of d1 and d2. From these figures, it can be seen that the characteristics of the thick-walled casing vibration acceleration signals under rubbing are almost the same as those of the thin-walled casing. The casing signals under rubbing have obvious periodic impact characteristics; the strength of this impact is modulated by the rotational frequency, and there also are obvious rotational frequency components in the wavelet envelope spectrums.

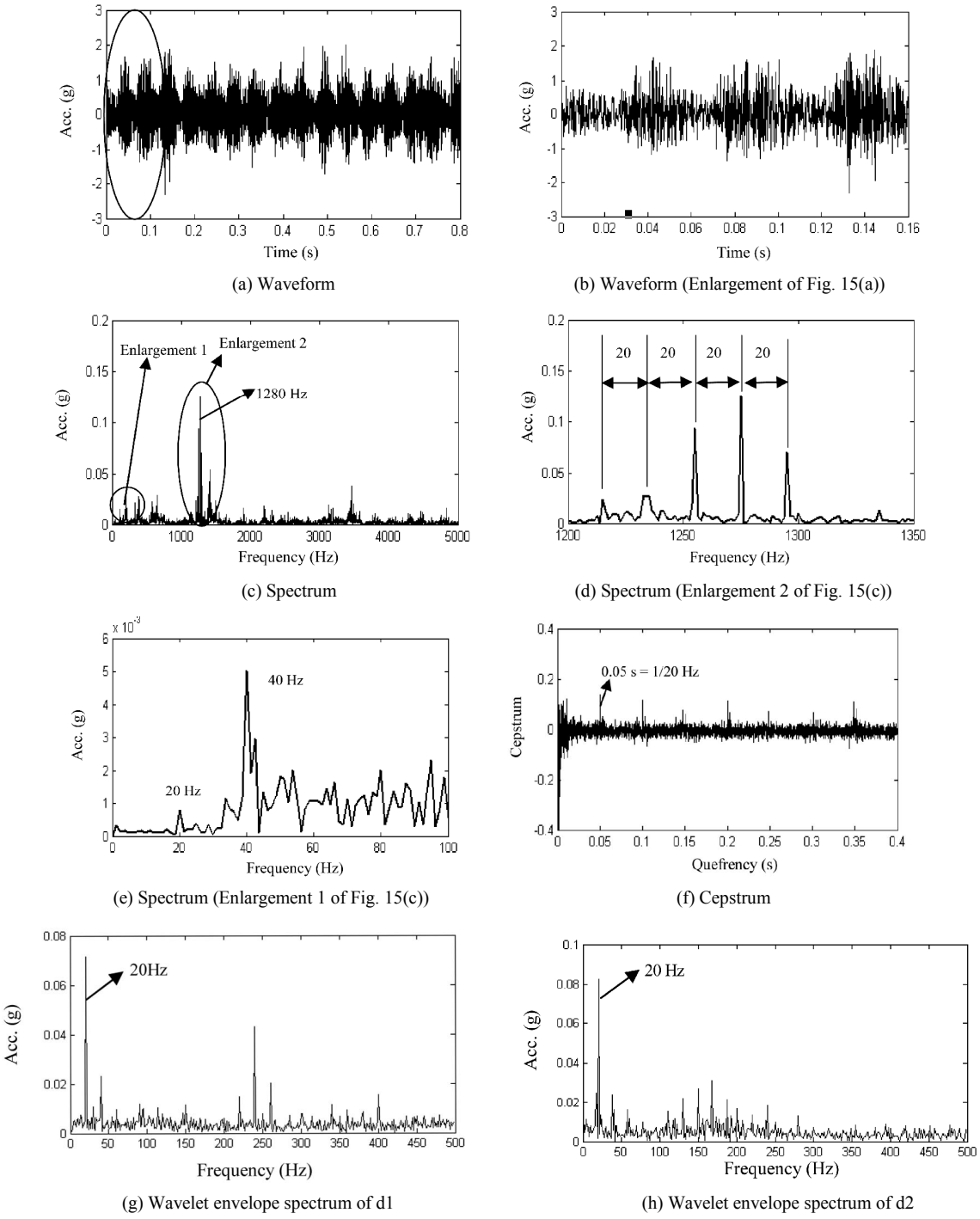

(a) Waveform

(b) Waveform (Enlargement of Fig. 15(a))

(c) Spectrum

(d) Spectrum (Enlargement 2 of Fig. 15(c))

(e) Spectrum (Enlargement 1 of Fig. 15(c))

(f) Cepstrum

(g) Wavelet envelope spectrum of d1

(h) Wavelet envelope spectrum of d2

Fig. 15. Characteristics analysis based on different measuring point signals.

2.5 Effect of rubbing intensity on rubbing characteristics

For comparing the effect of rubbing intensity on the characteristics of rubbing faults, the testing data of CH1 obtained from the single-point rubbing experiments conducted on July 27, 2011 was selected. The rotor–stator rubbing position was the vertical top of the thin-walled turbine casing. The experimental rotational speed was 1019 rpm = 17 Hz.

Figs. 14(a) and (b) show the time-domain waveforms. Figs. 14(c) and (d) show the frequency spectrum plots. Figs. 14(e) and (f) show the signal cepstrum. Figs. 14(g) and (h) show the wavelet envelope spectrum. From these figures, it can be seen that larger casing vibration acceleration is caused by serious rubbing, but the characteristics of different rubbing intensities are almost the same, and the characteristics of serious rubbing are clearer than those of light rubbing. This conclusion pro-

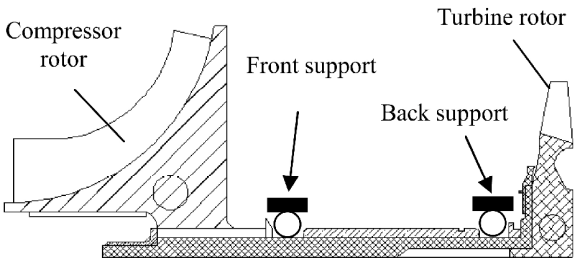

Fig. 16. Structural diagram of certain missile turbojet engine.

vides an important basis for rubbing recognition.

2.6 Effect of measuring point on rubbing characteristics

For analyzing the effect of measurement point location on rubbing characteristics, the compressor casing acceleration is analyzed under partial rubbing of the turbine casing. Data from the experiment conducted on April 29, 2013, i.e., data from the vertical upper measurement point on the compressor casing, was selected, and the experimental rotational speed was 1199 rpm = 20 Hz. Figs. 15(a) and (b) show the time-domain waveforms, and Fig. 15(b) shows an enlarged version of Fig. 15(a). Figs. 15(c)-(e) show the spectrum plots; Fig. 15(e) is enlargement 1 of Figs. 15(c) and (d) is enlargement 2 of Fig. 15(c). Fig. 15(f) shows the signal cepstrum, and Figs. 15(g) and (h) show the wavelet envelope spectrums. It can be seen that when the measurement point is far away the rubbing point, the signal amplitude decreases to some extent, but its characteristics are the same, namely, in the acceleration signal, there exist the blade-passage frequency and its multiple frequencies on both sides of which there are side bands with an interval equal to the rotating frequency. Furthermore, there are obvious quefrency components of the rotating frequency and its multiple frequencies in the cepstrum, and there also are obvious rotational frequency components in the wavelet envelope spectrums.

3. Characteristics analysis of certain real turbojet aero engine rubbing fault

3.1 Aero engine's structure and original vibration signals

A structural diagram of a certain missile turbojet aero engine is shown in Fig. 16. The aero engine is of the 0-2-0 support structure form, and it consists of a compressor rotor and a turbine rotor. There is only one measurement point on the middle casing above the front support. The casing vibration acceleration time history of an abnormal vibration is shown in Fig. 17. The aero-engine rotating speed rises from 30000 rpm to 50000 rpm, to 55000 rpm, to 58000 rpm, and then returns to 5000 rpm, to 30000 rpm finally. The sampling rate is 25.6 k.

3.2 Signal analysis

The changes in vibration acceleration with the changes in

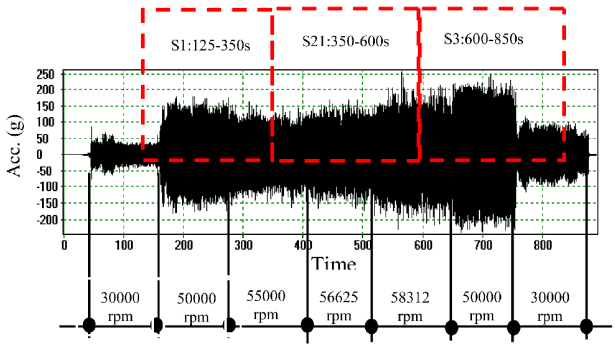

Fig. 17. Original data.

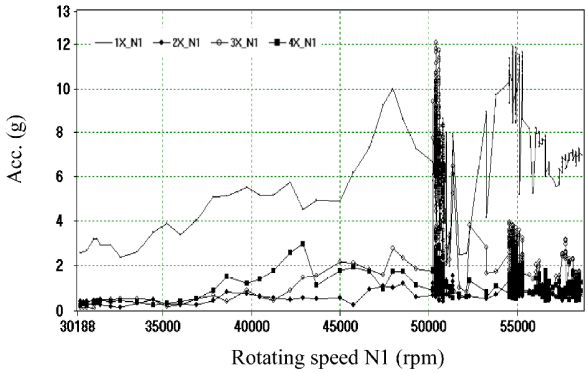

(a) 1×, 2×, 3×, and 4× components

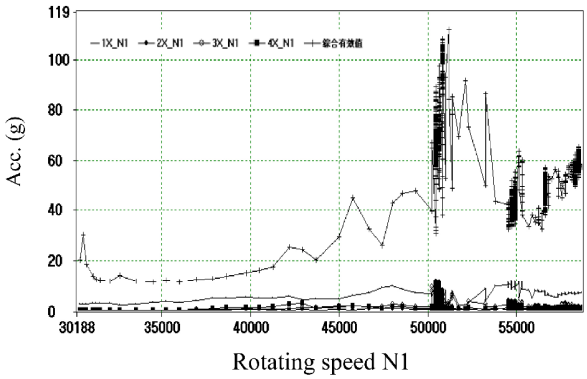

(b) 1×, 2×, 3×, 4×, and effective value

Fig. 18. Vibration–speed relationship.

rotating speed are plotted in Fig. 18. Fig. 18(a) shows a plot of the changes in the 1×, 2×, 3×, and 4× components with the changes in rotational speed, and Fig. 18(b) shows the changes in the 1×, 2×, 3×, and 4× components and the effective value with changes in the rotational speed. From Fig. 18, the following can be observed: 1) as the rotational speed increases from 30,000 rpm to 50,000 rpm, vibration acceleration increases gradually, but there is considerable fluctuation close to 50000 rpm; 2) All other rotating speeds except 50000 rpm, the 1× component is much larger than 2×, 3×, and 4× components, but near 50000 rpm, the 3× component is larger than 1× component, from Fig. 18(b), the vibration effective value near

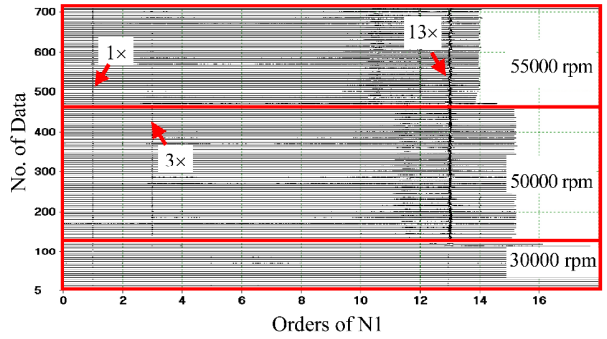

Fig. 19. The 3D waterfall plot of the S1:125-350 s.

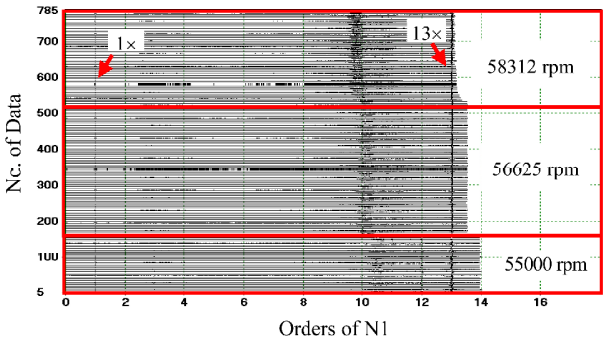

Fig. 20. the 3D waterfall plot of the S2:350-600 s.

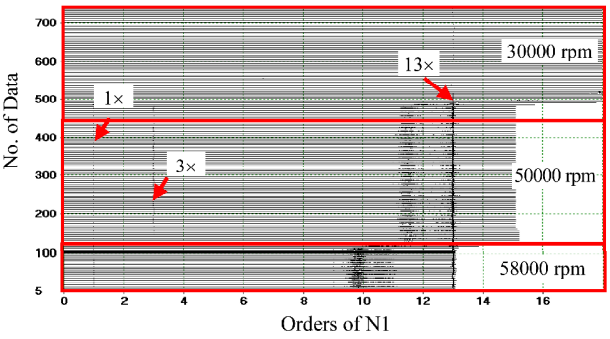

Fig. 21. the 3D waterfall plot of the S3:600-850 s.

50000 rpm reaches 110 g, and much larger than other speeds.

Here, the rotating speed is defined as N1. The whole process is divided into three segments: S1:125-350s, S2:350-600s, and S3:600-850s. Figs. 19-21, respectively, show the 3D waterfall plots of the three segments' vibration signals. From these plots, it can be seen that there is no 13 × N1 component as the rotational speeds are near 30000 rpm. However, as the rotational speeds rise over 50000 rpm, there is an obvious 13 × N1 component, and the number of the engine compressor blades is right 13.

Figs. 22 and 23 are the frequency spectrums of rotating speed 50812 rpm, and Fig. 23 is the longitudinal coordinate enlargement of Fig. 22. Figs. 24-26 are, respectively, the frequency spectrums of rotating speed 54750 rpm, 56625 rpm, and 58500 rpm. From Fig. 22, the 13×N1 component reaches 140g, and there is a sideband on both sides of the 13×N1

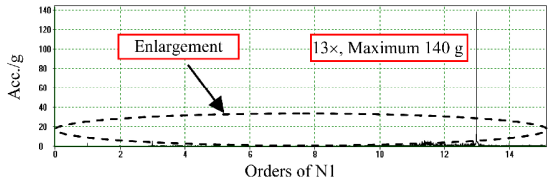

Fig. 22. Frequency spectrum (50812 rpm).

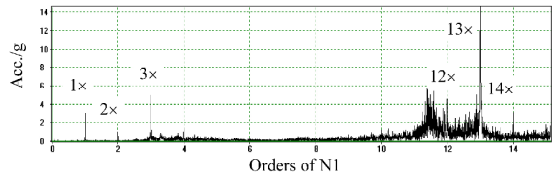

Fig. 23. Enlargement of Fig. 22.

Fig. 24. Frequency spectrum (54750 rpm).

Fig. 25. Frequency spectrum (56625 rpm).

Fig. 26. Frequency spectrum (58500 rpm).

component, and the sideband's interval is N1; and from Fig. 23, the 3×N1 component is obviously larger than the 1×N1 component. However, as shown in Fig. 24, the 13×N1 component is only 25 g as rotating speed 54750 rpm; only 20 g as rotating speed 56625 rpm as shown in Fig. 25; and only 40 g as rotating speed 58500 rpm as shown in Fig. 26. In addition, the 12×N1 component and the 14×N1 component near the 13×N1 component are all very small; in low frequency segments, the 1×N1 component is obviously larger than the 2×N1 component and 3×N1 component.

3.3 Conclusions of signal analysis

From the signals analysis, the blade-casing rubbing fault

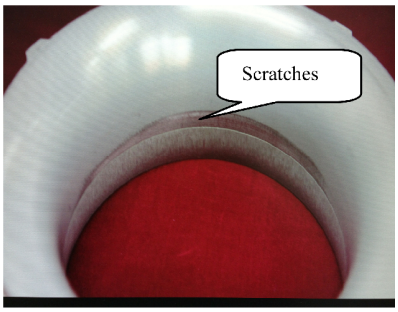

Fig. 27. Scratches in casing.

appears near 50000rpm. The main reasons are as follows:

(1) The vibration effective value reached 110 g near 50000 rpm; moreover there are considerable fluctuations in vibration.

(2) In a practical aero engine, the blade-passage frequency components, namely 13 × N1 components, probably come-from the gas exciting besides blade-casing rubbing. Usually the blade–passage component due to the gas exciting is not large; however, once rubbing appears, the blade-passage frequency component will sharply rise. Through the vibration signals analysis, it can been seen that near 50000 rpm, the 13×N1 components reach 140g; in addition, the sideband appears near the 13×N1 component. By contrast to the other rotating speeds, at 54750 rpm, 56625 rpm, and 58500 rpm, the 13×N1 components basically are all less than 40g. It shows that no rubbing faults appear at these rotating speeds, and the 13×N1 component mainly comes from the gas exciting, but no rubbing.

(3) Near 50000 rpm, in the low frequency segment of the spectrum, the 3×N1 component is obviously larger than the 1×N1 component; however, at other rotating speeds, the 1×N1 component is obviously larger than the 2×N1 and 3 ×N1components.

Finally, after disassembling the aero-engine, it was found that there were scratches on the centrifugal impeller and the centrifugal casing, as shown in Fig. 27; therefore, the correctness and effectiveness of the feature analysis about the rubbing fault in this study are strongly verified.

4. Conclusions

(1) The casing signals under rubbing have obvious cyclic impact characteristics; the impact frequency is the blade-passage frequency, which equals the product of the rotational frequency and the number of blades; the frequency spectrum contains the blade-passage frequency and its multiple frequencies. The rotor whirls due to an unbalanced force, so the strength of the impact is modulated by the rotating frequency. Consequently, there are families of sidebands on both sides of the blade-passage frequency and its multiple-frequencies, and the sidebands' interval equals the rotating frequency. There are obvious quefrency components of the rotational frequency and its multiple frequencies in the cepstrum. Compared with the signals under no rubbing, these characteristics disappear. The characteristics are very stable for different rubbing intensities, different casing thicknesses, and different measurement positions.

(2) In the low-frequency segment of the casing acceleration spectrum, there are more obvious rotating frequencies and their multiple frequencies under rubbing than under no rubbing. At present, aero engine fault diagnosis mainly focuses on the low-frequency segment, and the high frequency segment is usually ignored. However, the high-frequency segment contains more important information about aero engine rubbing faults.

(3) By analyzing the test data of a real aero engines, the accuracy and effectiveness of rubbing fault's characteristics determined in this study are strongly verified.

The research results presented in this paper have great significance and reference value for real aero engine fault diagnosis.

Acknowledgments

The author is very grateful to his graduate students Yu M Y, Cheng X Y, Zhao B, and Wang H F, who conducted many rubbing experiments; Wang J, who helped with translation. I especially thank Zhang H, an engineer with the Beijing Power machine Research Institute, for help with test data collection. This work is supported by the National Defence Research Program of China (No.613139) and National Natural Science Foundation of China (No. 61179057).

Reference

[1] A. Muszynska, Rotor-to-stationary element rub-related vibration phenomena in rotating machinery, *Shock and Vibration Digest*, 21 (1989) 3-11.

[2] Aeroengine design manual compiling committee, *Aeroengine design manual (19th part): rotor dynamics and whole-engine vibration*, Beijing, Aviation Industry Press (2000) 208-226 (in Chinese).

[3] A. Muszynska and P. Goldman, Chaotic responses of unbalance rotor bearing stator systems with looseness or rubs, *Chaos, Solitons and Fractals*, 5 (9) (1995) 1683-1704.

[4] B. C. Wen, X. H. Wu and Q. K. Han, *The nonlinear dynamics theory and experiments of rotating mechanism with faults*, Beijing, Science Press (2004) 149-151 (in Chinese).

[5] F. Chu and W. Lu, Experimental observation of nonlinear vibrations in a rub-impact rotor system, *J. of Sound and Vibration*, 283 (2005) 621-643.

[6] Y. L. Gao, Y. Li and D. Y. Wang, Experimental investigation of rotor - to - casing rubbing fault, *Aeroengine*, 4 (2002) 16-21 (in Chinese).

[7] S. G. Liu, J. Hong and M. Chen, Numerical simulation of aero-engine blade–casing rubbing process, *J. of Aerospace*

Power, 26 (6) (2011) 1282-1288.

[8] K. Turner, M. Adams and M. Dunn, Simulation of engine blade tip-rub induced vibration, *Proceedings of GT2005*, Reno-Tahoe, Nevada, USA (2005).

[9] G. Chen, C. G. Li and D. Y. Wang, Nonlinear dynamic analysis and experiment verification of rotor-ball bearings-support-stator coupling system for aero-engine with rubbing coupling faults, *J. of Engineering for Gas Turbines and power*, 132 (2010) 022501-1 — 022501-9.

[10] S. G. Liu, J. Hong and M. Chen, Numerical simulation of the dynamic process of aero-engine blade-to-case rub-impact, *J. of Aerospace Power*, 26 (6) (2011) 1282-1288.

[11] R. J. Williams, Simulation of blade casing interaction phenomena in gas turbines resulting from heavy tip rubs using an implicit time marching method, *Proceedings of ASME Turbo Expo 2011*, Vancouver, British Columbia, Canada (2011).

[12] S. K. Sinha, Non-linear dynamic response of a rotating radial Timoshenko beam with periodic pulse loading at the free-end, *International J. of Nonlinear Mechanics*, 40 (2005) 113-149.

[13] K. Turner, M. Adams and M. Dunn, Simulation of engine blade tip-rub induced vibration, *Proceedings of GT2005*, Reno-Tahoe, Nevada, USA (2005).

[14] K. Turner, M. Dunn and M. Padova, Airfoil deflection characteristics during rub events, *J. of Turbomachinery*, 134 (2012) 011018-1-011018-7.

[15] H. Qiu et al., Wavelet filter-based weak signature detection method and its application on rolling element bearing prognostics, *J. of Sound and Vibration*, 289 (4) (2006) 1066-1090.

G. Chen is a professor of the College of Civil Aviation, Nanjing University of Aeronautics and Astronautics, Nanjing, P. R. China. He is currently engaged in whole aero engine vibration, rotor-bearing dynamics, rotating machine fault diagnosis, pattern recognition and machine learning, signal analysis, and processing.